Central engine of a gamma-ray blazar resolved through the magnifying glass of gravitational microlensing

X-ray data analysis

The X-ray data set used in this work includes SWIFT XRT, SWIFT BAT and INTEGRAL ISGRI data, covering 0.3-500 keV energy range, as well as the previously published results of ASCA, Chandra and XMM-Newton telescopes.

The SWIFT/XRT spectral and temporal data analysis was performed using the online web interface provided by the UK Swift Science Data Centre at the University of Leicester, [31]. PKS 1830-211 was observed with SWIFT/XRT during September 2010 – April 2011 for 33 ksec in total. The XRT spectrum in the 0.3-10 keV energy range is well fit with a simple absorbed power law model with spectral index $\Gamma = 1.19 \pm 0.05$ and neutral hydrogen column density $N_H = (1.22 \pm 0.07) \cdot 10^{22} \mathrm{cm}^{-2}$. The XRT spectrum is shown in Fig. 10 with the orange data points. The de-absorbed power law spectral model is shown with the grey line.

The Swift/BAT light curve and spectrum were produced using the web-based tool provided by the Swift/BAT team [32]. The SWIFT/BAT data cover the time range from February 2005 to August 2014. The BAT spectrum is well fit with a power law model with the photon index $\Gamma = 1.46 \pm 0.07$.

The INTEGRAL/ISGRI data cover the period from March 2003 to April 2014 with an overall exposure of 16 Msec in the 20-500 keV energy range. We have performed the analysis of the data with the help of the OSA 10.0 software[1] provided by the INTEGRAL Science Data Centre [33]. We have used the `ibis_science_analysis` tool up to the image reconstruction ("IMA") step, producing images in 6 energy bands (20-40 keV, 40-60 keV, 60-100 keV, 100-200 keV, 200-500 keV and 500-990 keV). The mosaic image of the sky region around the source in the 20-40 keV band is shown in Fig. 1. The mosaic of all images was subsequently used for the spectral extraction. PKS 1830-211 is located close to the crowded Galactic Center region, containing many point sources as well as the diffuse emission of the Galactic Disk. The ISGRI coded mask detection technique results in large residuals in the images, caused by the non-perfect removal of "ghosts" of the detected sources. This complicates the estimate of the background level on top of which the source is detected. We have estimated the background in the mosaic images in each energy band from the concentric rings of different size around the source. Our flux estimate is dominated by the systematic error due to the uncertainty in the background subtraction. We have estimated this uncertainty as the standard deviation of the source's intensity for different choices of the regions for background estimate. The INTEGRAL/ISGRI spectrum of the source calculated using this procedure is shown in Fig. 10. It is consistent with the spectrum extracted from a shorter 2.5 Msec exposure previously reported in [34]. Fig. 2 shows the 20-60 keV light curve of the source.

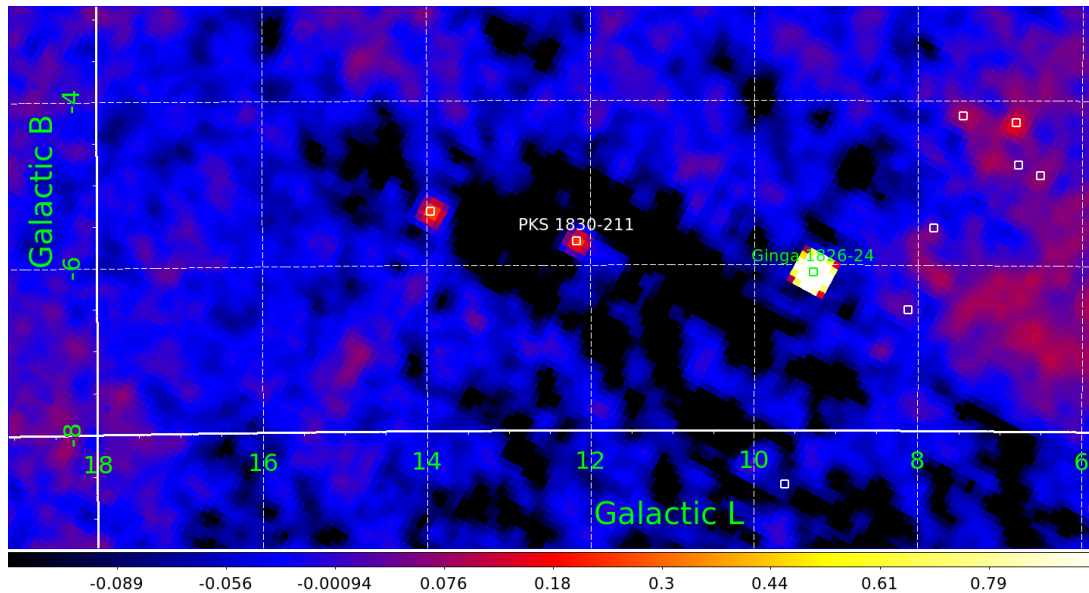[1]See e.g. http://isdc.unige.ch/integral/osa/10.0/README_osa

Figure 1: INTEGRAL/ISGRI intensity image of the sky region around PKS 1830-211 in the 20-40 keV band. The green box marks the position of Ginga 1826-24 – one of the bright nearby sources, the white boxes mark the positions of PKS 1830-211 and few other catalogue sources.

Gamma-ray data analysis

In this work we used all publicly available data from the Fermi/LAT Pass 7 dataset[2] over the time period from August 2008 till September 2014. The data were processed using the procedures described in the Fermi Analysis Threads[3] using the Fermi Science Tools[4] v9r33p0. We have considered events of the "Source" (P7REP_SOURCE) class, falling in the circle with the radius of 18° around the source position (RA = 278.416°, Dec = −21.061°). We further applied the zenith angle cut of 105° and selected only the good-quality data by applying the "DATA_QUAL==1 && LAT_CONFIG==1 && ABS(ROCK_ANGLE) < 52" filter at $gtmktime$ step. The light curves were obtained using the likelihood analysis method, fitting the spectral / spatial model of the observed region to the data in each time bin. The model of the sky region used in the likelihood analysis included all sources from the 2FGL catalogue [2] as well as the latest available templates for the galactic and extra-galactic diffuse backgrounds (`gll_iem_v05_rev1.fit` and `iso_source_v05_rev1.txt`). The spectra of all sources were assumed to be power laws in energy with free normalizations and with slopes fixed to the best-fit values over the entire observational time range.

To get the optimal timing coverage of the variability, we produced the light curves using variable time bin sizes. The length of each time bin was determined from the aperture photometry light curve of the source (RA = 278.416°, Dec = −21.061°, Rad = 1°, E > 100MeV), binned using the signal to noise ratio SNR=6 with the help of the $gtbin$ tool. For each bin of the

---

[2] http://fermi.gsfc.nasa.gov/ssc/data/analysis/documentation/Pass7REP_usage.html

[3] http://fermi.gsfc.nasa.gov/ssc/data/analysis/scitools/

[4] http://fermi.gsfc.nasa.gov/ssc/data/analysis/software/

light curve we estimated the significance of source detection based on the Test Statistics (TS) value [35]. The significance roughly corresponds to $\sqrt{TS}$. Bins with the significance less than 3σ ($TS < 10$) are considered to be weak detections.

The 30 MeV – 60 GeV spectral data points shown in Fig 10 were obtained using the binned likelihood analysis with the `BinnedAnalysis` python module. At low ($\lesssim 100$ MeV) energies only events from the higher quality "Clean" class were considered and the size of the analysis region was extended to $\approx 21°$, to take into account wider point spread function of LAT in this energy range.

Timing analysis of the gamma-ray data

The gamma-ray light curve of PKS 1830-211 shown in Fig. 2 exhibits several activity episodes, highlighted by the grey vertical bands. The two brightest flaring periods are around MJD dates 55500 and 56100 and the two weaker flares are seen at MJD=55160 and 56870. A more detailed view of these flaring episodes is shown in Fig. 1 of the main text.

To investigate the timing properties of the signal, we have computed the structure function (SF) [36, 37, 38, 39] of the entire light curve in the 0.1-510 GeV band (from MJD 54688 to 56979, almost 2300 days in duration). The SF of the light curve $f(t)$, computed at the time lag τ, is defined as [36]

$$SF_f(\tau) = \langle (f(t+\tau) - f(t))^2 \rangle \tag{1}$$

where the averaging $\langle \rangle$ is over the time t. The SF provides a measure of variability of the source on the time scale τ and is a time domain analogue of the power spectrum. It carries the same information as the autocorrelation coefficient $\mathcal{R}(\tau) = \langle f(t)f(t+\tau) \rangle$. Similarly to the power spectrum, the structure function of the "red noise" variability of AGN has a power law shape in the time delay range from the minimal variability time scale up to the maximal time scale of the timing measurements. Correlated variability on a characteristic time scale τ_c produces "dips" superimposed on the red noise power law. A strictly periodic variability would produce a dip down to $SF_f(\tau_c) = 0$. For a deeper discussion of the SF properties and caveats we refer the reader to [40].

Our SF analysis is based on the source light curve binned with 2 days wide time bins. To estimate the uncertainties of the SF, we simulated 200 light curves, based on the original fluxes and their uncertainties in each time bin.

The SF shown in Fig. 3 features several dips at different time lags. The dips at $\tau \approx 300$, 600 and 900 days are attributed to the intervals between different flaring periods. They can not be attributed to the gravitational time delay, as the intervals between the subsequent flaring episodes are not the same. In addition to the dips corresponding to the time intervals between the flaring episodes, there are two more dips at $\tau_\gamma = 21^{+2}_{-2}(stat)^{+2}_{-3}(sys)$ and $\tau_{rep} = 76^{+7}_{-7}(stat)^{+18}_{-8}(sys)$ days. The dips are detected as deviations of the SF from the red noise power law model. The time lag τ_γ is detected with the significance of 4.8σ, while τ_{rep} is detected with the significance of 4.9σ. The 68% statistical uncertainties on the positions of the dips were determined from the scatter in the positions of the points of largest deviation from the powerlaw models in the simulated SFs. The systematic uncertainties were estimated as full widths of the dip profiles at half maxima.

We have verified the results of the SF analysis with an alternative method based on the wavelet analysis of the light curve [41]. A potential advantage of the wavelet analysis is that
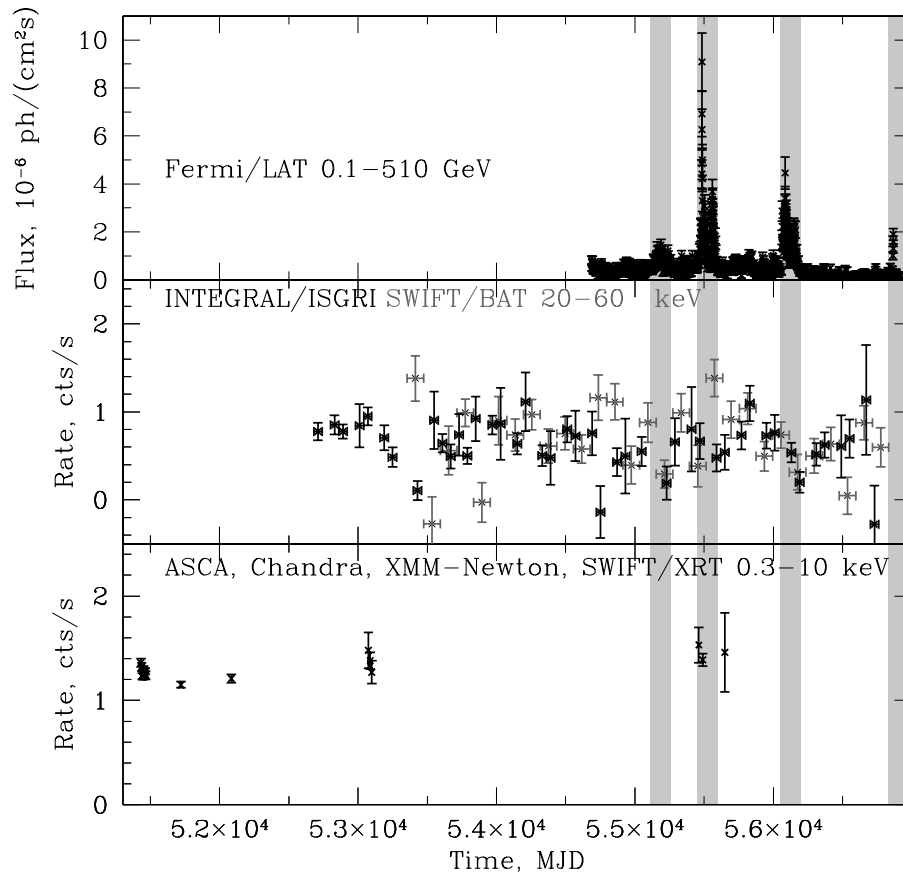
Figure 2: Light curves of PKS 1830-211 in different energy bands. Errorbars correspond to 68% confidence intervals. The Fermi/LAT data are shown in the top of the figure, IN-TEGRAL/ISGRI and SWIFT/BAT are given in the middle panel and the lower-energy X-ray measurements (a compilation of measurements by ASCA, Chandra, XMM-Newton and SWIFT/XRT telescopes) are displayed in the bottom panel. Vertical shaded bands mark the time intervals of flaring episodes.
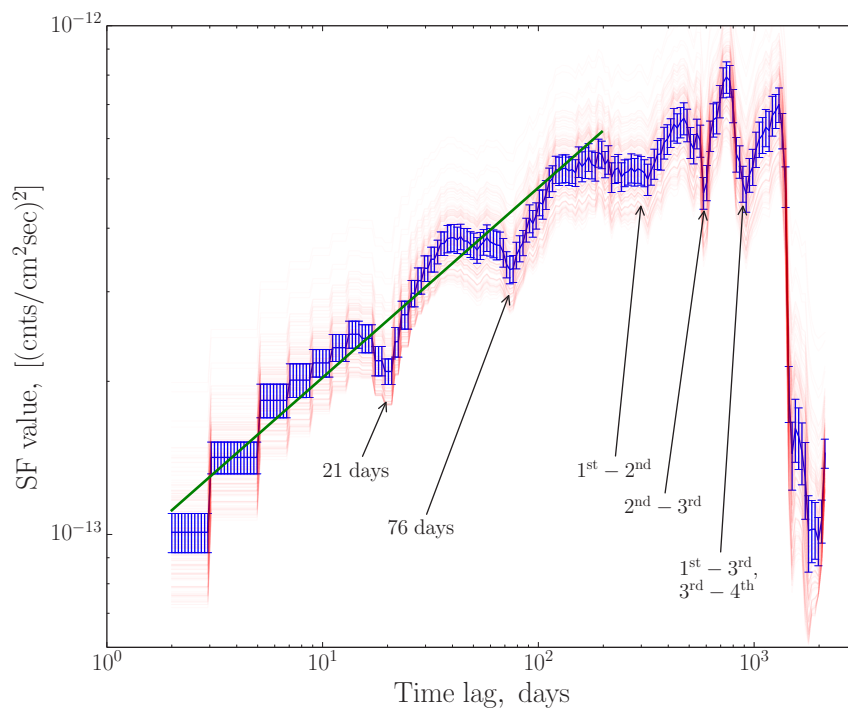
Figure 3: The structure function of the γ-ray light curve. The errorbars, estimated from Monte-Carlo simulations, correspond to 68% confidence intervals. Light red shows the structure functions of the separate simulated light curves, which were used to estimate the uncertainties, green line shows the red noise component of the SF. The arrows mark dips at the time intervals between different flaring episodes, as well as at the two characteristic time scales τ_γ (21 d) and τ_{rep} (76 d).
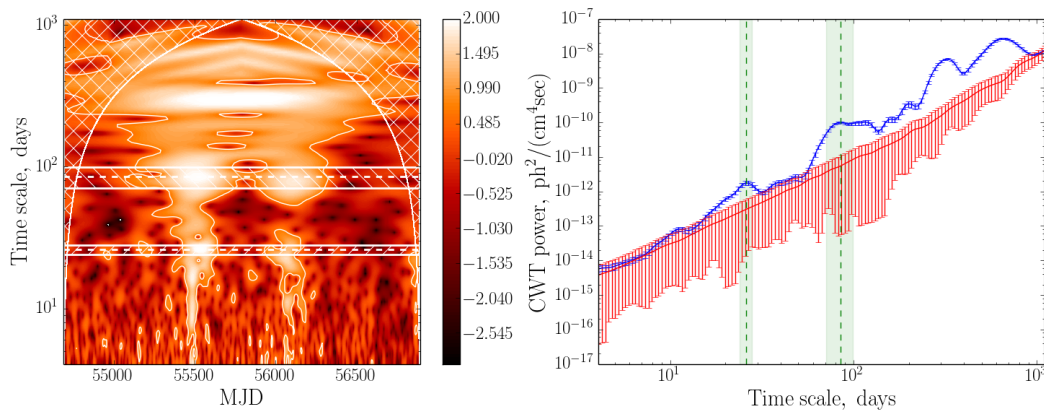
Figure 4: *Left:* CWT power spectrum of the γ-ray light curve. The colour scale shows the log_{10} of the ratio of the CWT power of the signal and the red noise. Hatched regions are affected by the edge effect during the CWT computation. White contours mark the regions which are at least 3 standard deviations above the red noise component. Horizontal dashed lines and hatched ranges show the τ_γ^{CWT} and τ_{rep}^{CWT} time scales. *Right:* Time averaged CWT power spectrum (blue) and of the red noise (red) with 68% errorbars estimated from Monte-Carlo simulations. Vertical dashed lines and shaded regions mark the τ_γ^{CWT} and τ_{rep}^{CWT} time scales.

it allows not only detection of the characteristic time lags in the signal but also a study of possible long-term variations of these time lags. To allow a direct comparison with the results of Ref. [41], we used the Morlet wavelet as a base function and performed a continuous wavelet transform (CWT) of the data in order to derive a time-dependent CWT power spectrum. We additionally computed an average CWT spectrum over the entire observation time span. We have estimated the uncertainty on the power spectrum using a set of simulated source light curves, scattered within the error bars of the real data points.

Similarly to the SF, the CWT power spectrum contains a "red noise" powerlaw component. We have estimated the uncertainty of the red noise level from a set of simulated light curves computed for the reference red noise spectrum, passing through lowest power data points of the wavelet spectrum. The ratio of the signal CWT spectrum to the red noise spectrum is shown in the left panel of Fig. 4. The upper left and right corners of the left panel of Fig. 4 are affected by the edge effects related to the finite time span of observations. These regions are also marked in the Figure with the hatches. The right panel of Fig. 4 shows the time-averaged CWT power spectrum.

The wavelet power spectrum has several peaks at the time scales larger than 100 days, corresponding to the time intervals between the flaring episodes. There are also two peaks at the time scales $\tau_\gamma^{CWT} = 26_{-2}^{+2}(stat)_{-4}^{+9}(sys)$ and $\tau_{rep}^{CWT} = 85_{-14}^{+14}(stat)_{-12}^{+46}(sys)$. The significances of detection of these time scales, estimated from the excess over the red noise level, are 5.2σ and 18.7σ. Similarly to the SF analysis, we have estimated the statistical uncertainty of the measurement from the scatter in the CWT maxima positions calculated for the simulated light curves. The systematic uncertainties were estimated from the width of the peaks at the half
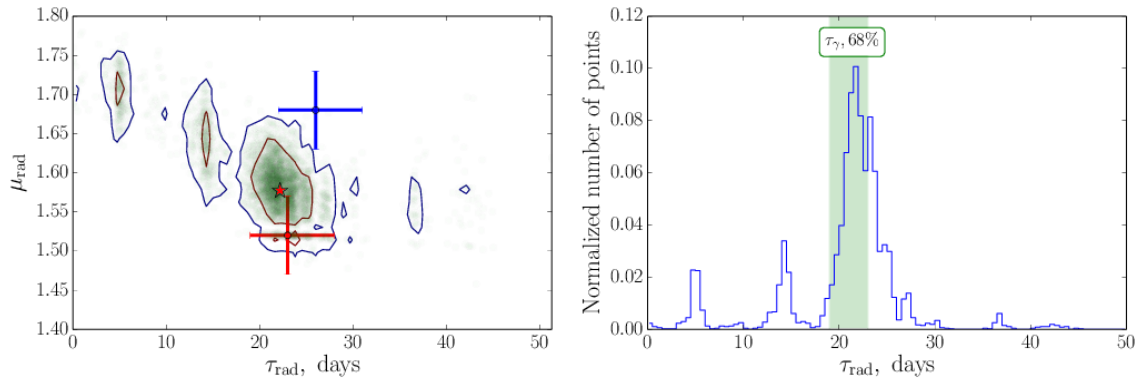
Figure 5: *Left:* Time delay and magnification factor ratio derived from the re-analysis of the entire radio light curve from Ref. [28]. The best-fit values are marked with the red "star" symbol. The 68% and 95% confidence contours are plotted in red and blue. The original values from [28] for the full (red data point) and limited (blue data point) data sets are also plotted. *Right:* The normalised histogram of the derived values of τ_{rad} compared to the 68% confidence range for τ_{γ} (green shaded region), obtained above.

maxima. The time scale τ_{γ}^{CWT} is consistent with τ_{γ} and the time scale τ_{rep}^{CWT} is consistent with τ_{rep} within errorbars. Both time scales τ_{γ} and τ_{rep} systematically re-appear in the flaring episodes of the source. Thus, they both could potentially correspond to the gravitational time delay between the two images of the source.

The gravitational time delay is an achromatic phenomenon and as such it should be the same for the signal in different wavelength ranges. To understand which of the two time scales corresponds to the gravitational time delay, we have reanalysed the radio light curves of the two source images reported in [28], following the same procedure, as was adopted there. The original publication [28] quotes two values of the gravitational time delay in PKS 1830-211: 23 days, derived for the entire radio light curve, and 26 days, derived for the subset of radio observations around a flare. The value of the magnification ratio $\mu_{rad} = 1.52 \pm 0.05$ corresponds to the 23-day time delay. The confidence range on τ_{radio} corresponding to this value of μ_{rad} is not given. We have simulated a number of light curves ($\simeq 4000$), based on the values and uncertainties in the original light curves from [28] and applied the procedure described in [28] to find the confidence range $\tau'_{rad} = 22 \pm 3$ days (the prime marks our estimate as opposed to the the estimate from [28]). The confidence ranges on the values of τ'_{rad} and μ'_{rad} derived in this way are shown in Fig. 5.

The radio band time delay τ'_{rad} is consistent with the time scale τ_{γ}. To the contrary, the time scale τ_{rep} is inconsistent with the radio time delay at more than 3σ level. This indicates that it is the time scale τ_{γ} which should be identified with the gravitational time delay. Comparison of different measurements of the gravitational time delay derived from the radio and γ-ray data is shown in Fig. 6.

The flares shown in Fig. 1 of the main text are characterised by short variability time scales. To estimate the minimal variability time scale we focused on the brightest flare that happened
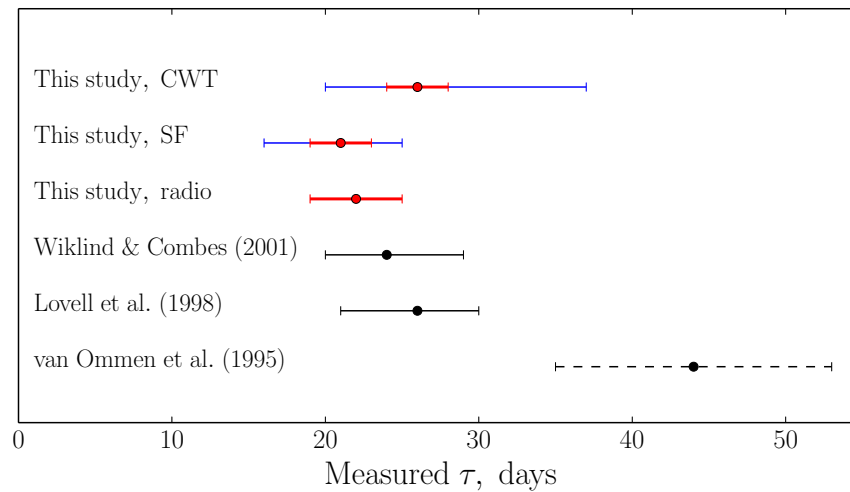
Figure 6: Comparison of the values of the gravitational time delay, as measured from the radio [42, 43, 28] and γ-ray data (this work). For the latter, both statistical (68% confidence intervals, red) and systematic (blue) error bars are shown. We also plot the time delay value we derived from the re-analysis of the source radio light curves from [28]. The result of van Ommen et al. (1995) [42] is shown with a dashed line, as it was later put into question in [28].

on MJD ≈ 55484.5. To study this flare in more detail, we produced its light curve in the 0.1-510 GeV energy band with a constant signal-to-noise ratio SNR = 4. We have fitted the flare profile with the exponential rise/decay model, as shown in Fig. 7. The derived rise and decay times are $\tau_{\mathrm{rise}} = 0.49 \pm 0.15$ days and $\tau_{\mathrm{decay}} = 1.20 \pm 0.24$ days.

Magnification factor ratio

We used three sharpest bright flares in the 0.1-510 GeV light curve at MJD 55485, 55561 and 56867 to determine the magnification factor ratio. For each episode we computed the ratio between the fluxes of the primary and delayed components, as a function of the assumed time delay. The results are plotted in Fig. 8. The sharp flares allow to avoid the ambiguity due to the overlap with the subsequent variability of the source; still the values of μ_γ derived from the MDJ 56867 episode do suffer from contamination by the subsequent flares of the source.

The derived values of μ_γ are significantly larger than the value of the magnification factor ratio in the radio band – $\mu_{rad} \approx 1.52 \pm 0.05$ [28]. The average $\mu_\gamma \approx 3.1$ deviates from μ_{rad} by $\approx 3\sigma$. We have verified the significance of this deviation by simulating the γ-ray lightcurve as a sum of two lightcurves repeating each other with a time delay τ'_{rad} and with the flux ratio of the two components equal to μ'_{rad}. The counts in each time bin were taken from two Poissonian distributions. We have measured the flux ratio of the two flaring components of the simulated lightcurves to find how often the value $\mu \geq 3.1$ occurs in result of the up-fluctuation of the count rate of the weaker component and/or down-fluctuation of the stronger component. We
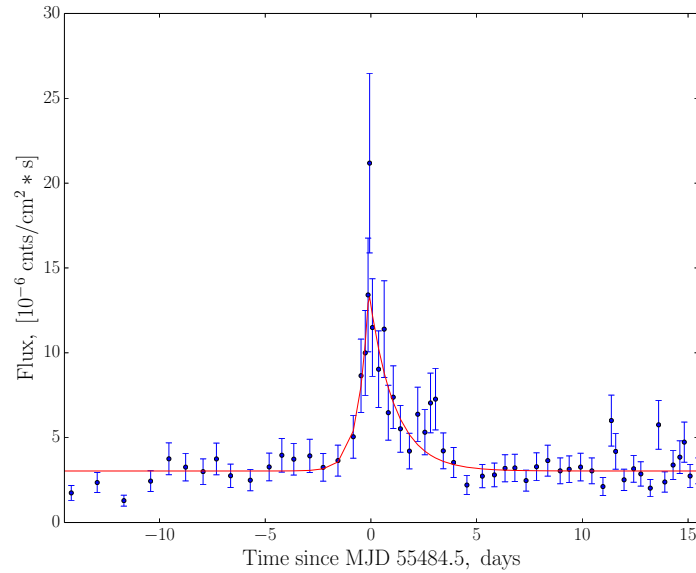
Figure 7: Zoom into the brightest flare of PKS 1830-211, observed on MJD $\approx$ 55484.5. The red line shows results of the fit with the exponential rise/decay model of the time interval ± 10 days around the flare.

have found that this occurs in less than 0.1% of simulations. This demonstrates that the high magnification ratio observed in γ-rays could not be related to the statistical fluctuations of the γ-ray signal during the source flaring episodes.

The γ-ray magnification factor ratio μ_γ appears to be variable from flare to flare. For the flare on MJD 55561 μ_γ is marginally consistent with μ_{rad}, whereas on MDJ 55484 $\mu_\gamma = 6.5 \pm 1.5$. The chance probability of such change is $\approx 0.7\%$.

Numerical simulations of caustics maps

We have verified our conclusions on the influence of the microlensing on the γ-ray lightcurve and on the small size of the γ-ray emission region using the numerical simulations of the microlensing effect. We have generated the microlensing caustics maps implementing the inverse ray shooting method [44, 45, 46] on the GPU using the cross-platform OpenCL[5] standard, which was suggested to have the best efficiency/simplicity combination [47]. The caustics maps were simulated in the 0.2x0.2 pc region in the source plane for the distribution of the point-mass lenses (stars) following the Initial Mass Function (IMF) from [48]. The total amount of stars-lenses in our simulation was controlled by the parameter Σ, representing an average amount of lenses per πR_E^2 area. Throughout the simulations the value of Σ varied in the range [0.2,1], which resulted in $\approx 160 - 800$ simulated stars-lenses in each run.

We sampled 20 magnification curves for each simulated caustics maps by taking pairs of randomly oriented straight line slices of the maps. Each magnification curve was then convolved
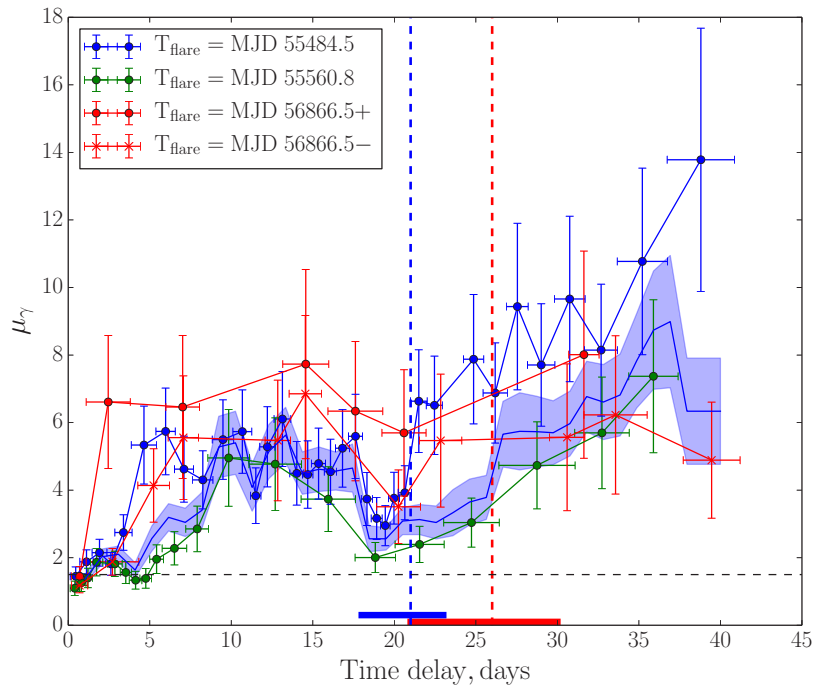
---

[5]https://www.khronos.org/

Figure 8: The magnification factor μ_γ of PKS 1830-211, measured in the 0.1-510 GeV energy band (errorbars correspond to one standard deviation). The μ_γ was computed for the three sharpest flares of the source. Dashed vertical lines and scales mark the time delays of 26^{+4}_{-5} (red) and 21^{+2}_{-3} (blue) days, derived from the radio data [28] and present analysis correspondingly. For the flare of MDJ 56866 it is not clear, whether the leading or delayed flare was magnified, so μ_γ was separately computed for T > MDJ 56866 (plus sign) and T < MDJ 56866 (minus sign). The blue line and shaded region show the weighted average of the magnification derived from all flares and its uncertainty. Horizontal dashed line represents $\mu_{rad} = 1.52 \pm 0.05$ [28].
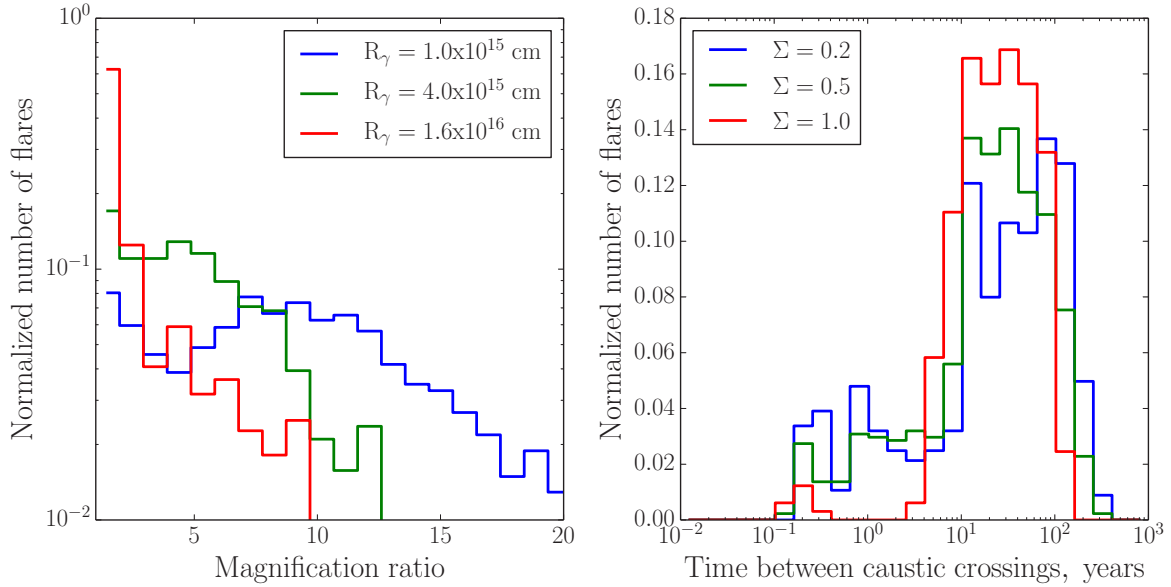
Figure 9: *Left:* The distribution of magnification ratios during caustic crossing events for different source sizes. The position of the peak of the distribution roughly scales as $1/\sqrt{R_\gamma}$. *Right:* The distribution of time intervals between subsequent caustic crossing events.

with the source surface brightness profile which we assumed to be a uniform disk of fixed size. The magnification ratio curve was taken to be the ratio of the two magnification lightcurves. We have searched for spikes in the simulated magnification ratio lightcurves by applying a filtering based on the Continuous Wavelet (CWT) transform with the Ricker (or "Mexican hat") wavelet base function, which is well-suited for the detection of the sharp spikes in the data. Setting the width parameter of the wavelet to $0.25\,R_\gamma/v_{rel}$ allowed us to reliably identify most of the caustic crossing events in our simulation. We then used the caustic crossing events identified in this way to estimate the maximal magnification ratio during the caustic crossings and the rate of the caustic crossing events.

The simulated distributions of the magnification ratios μ_{ml} and of the time intervals between caustic crossings are shown in Fig. 9. We fixed the density of the lenses at $\Sigma = 0.5$ for the study of the dependence of the maximal magnification on the source size. The source size was fixed ($R_\gamma = 10^{15}$ cm) for the study of the rate of the high-magnification episodes. The observed γ-ray maximal magnification ratio is $\mu_\gamma = \mu_{ml} \times \mu_r$ if the strong microlensing event occurs in the brighter of the two source images or $\mu_\gamma = \mu_{ml}/\mu_r$ if the dimmer of the two images passes behind the microlensing caustic. In the particular case of Fig. 9, $\mu_{ml} \times \mu_r$ was plotted to mimic the observed magnification factor behaviour.

From Fig. 9 one could see that if the size of the source is too small $R_\gamma < 10^{15}$ cm, typical magnification factor ratio increase during caustic crossings is larger than observed. Otherwise, if the source size is too large $R_\gamma > 10^{16}$ cm, the typical μ_γ values are smaller than observed. The estimate of the source size from the maximal magnification factor depends on a number of

parameters which are not directly measured, such as e.g. the average mass of the micro-lens. Thus, it could not be made more precise then "by order-of-magnitude".

The distributions of the time intervals between subsequent events of rapid magnification indicate that the chances to see 2 microlensing events over the 6 years of Fermi/LAT observations remain high for all the values of Σ we have tested, although they are smaller for higher values of Σ (7% for $\Sigma = 1$ vs. 25% for $\Sigma = 0.2$). This is consistent with the Fermi/LAT observational data.

Opacity with respect to pair production

The low-energy photons of energy ϵ, originating from the accretion flow or as a part of the overall emission from the PKS 1830-211 jet, may interact with the gamma rays of energies E_γ, resulting in their absorption, if $E_\gamma > E_{thr} \simeq 10^8 \Gamma^2 (\epsilon/1 \text{ keV})^{-1}$ eV. The density of the low-energy photons in an isotropically emitting source of the size R_X and luminosity L_X is $n_X = L_X/(4\pi R_X^2 c\epsilon) \simeq 10^9 \left(L_X/10^{46} \text{ erg/s}\right) \left(R_X/10^{16.5} \text{ cm}\right)^{-2} (\epsilon/100 \text{ keV})^{-1}$ cm^{-3}. The optical depth of the source w.r.t. the pair production is $\tau = R_X n_X \sigma_{\gamma\gamma} \simeq 0.3 \left(L_X/10^{46} \text{ erg/s}\right) \left(R_X/10^{16.5} \text{ cm}\right)^{-1} (\epsilon/100 \text{ keV})^{-1}$, where $\sigma_{\gamma\gamma} \simeq 10^{-25}$ cm^2 is the peak value of the pair production cross-section. The X-ray luminosity of the source is an order of magnitude lower than its γ-ray luminosity (see Fig. 10). Thus the compact emission region at the base of the jet of a $10^{8.5} M_\odot$ black hole is transparent for the 100 MeV γ rays pair producing on the 100 keV X-rays (assuming $\Gamma \simeq 10$), even if the X-ray source size saturates the lower bound derived from the non-detection of the microlensing in X-rays.

The spectrum of the source in the hard X-ray energy band is a power law with $L_\epsilon \sim \epsilon^{0.5}$ (Fig. 10), so that the optical depth of the source grows as $\tau \sim \epsilon^{-0.5} \sim E_\gamma^{-0.5}$ if the X-ray / hard X-ray source size is energy independent. The opacity of the source reaches at most $\tau \lesssim 3$ in the energy range $E_\gamma \sim 10$ GeV in which γ-rays produce pairs in interaction with the X-ray photons. The opacity does not grow further in the energy range $E \gg 10$ GeV, because the source spectrum in the X-ray range is $L_\epsilon \sim \epsilon^1$, so that $\tau_{\gamma\gamma} \sim \epsilon^0$, see Fig. 10.

The constraint on the X-ray emission region size $R_X \gtrsim R_E^* \simeq 4 \times 10^{16}$ cm, imposed by the non-detection of microlensing in X-ray light curve of PKS 1830-211, thus makes the source sufficiently transparent for us to see the gamma rays of ~ 10 GeV energies.

Location of the compact source within the blazar

The microlensing data reported in this paper constrain the size, but not directly the location of the γ-ray emission region within the supermassive black hole (SMBH) – jet system. The "natural" location of the compact γ-ray emission region of the size $\leq 10 - 100 R_g$ is inside the AGN central engine, in the region of generation / collimation of the AGN jet. However, it is possible that an isolated compact emission region develops in the jet far away from the central engine, e.g. due to magnetohydrodynamic instabilities of the jet flow.

The jets of the Active Nuclei are know to contain inhomogeneities in their structure, known as "knots"; an example of these is the HST-1 knot in the M87 radio galaxy. The observed VHE emission might be related to those knots rather than to the central black hole itself. In case of M87 several interpretations of the VHE emission were brought forward, including also HST-1 as
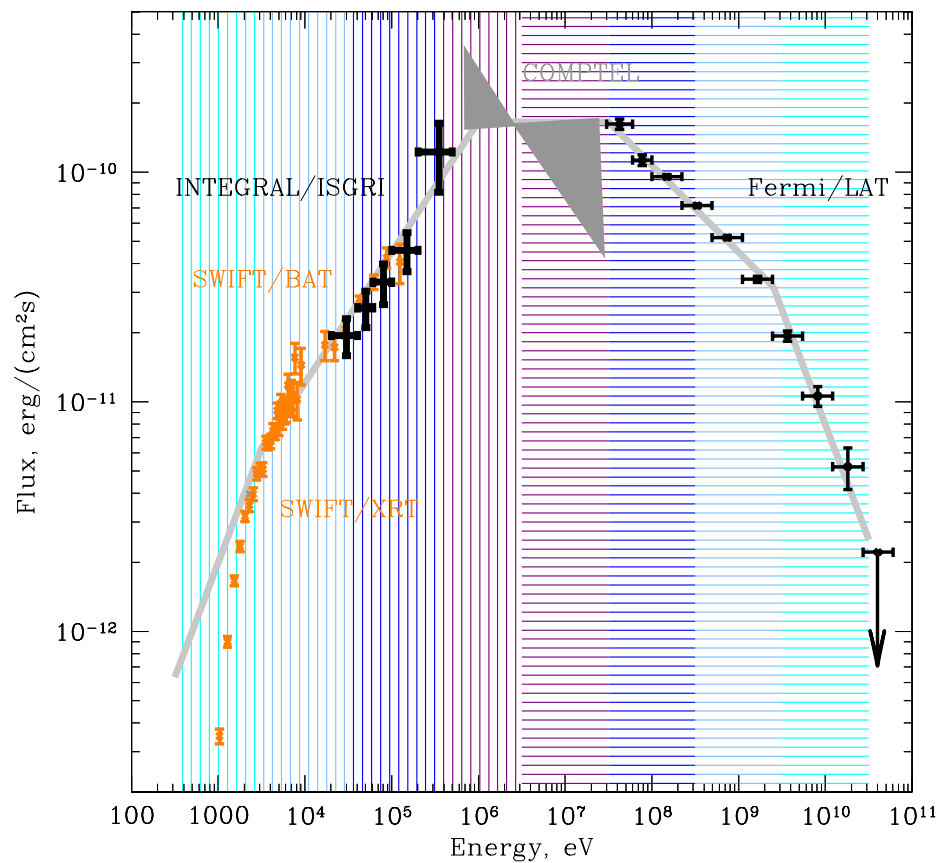
Figure 10: The X- to γ-ray spectrum of PKS 1830-211 (68% confidence range errorbars). Vertical/horizontal hatched bands of the same colour show the energy ranges of γ-rays and of the X-ray photons which interact most efficiently with each other via the pair production.

a possible source of the emission [49, 50, 51]. However, such distant structures have difficulties as the candidates for the observed VHE emission from the source due to the very short, daily variability time scales, detected in it [49, 52]. Typical transverse size of the jet with an opening angle Θ_{jet} grows linearly with the distance R from the AGN central engine as $R\Theta_{jet}$, reaching parsec scales at the distances of 10-100 pc (comparable to the distance of the HST-1 knot in M87). Constraints on the source size derived in this paper explicitly rule out the possibility that emission from such distant regions of the jet dominates the γ-ray emission power.

Several studies have proposed models involving compact structures in the jet moving relativistically with respect to its reference frame [53, 54, 55, 56]. In these models the structures as small as $\sim 10^{14}$ cm can be formed at distances of the order of $\sim 100R_g$ from the central SMBH. Such "jet-in-jet" models are, however, disfavoured by observations of another nearby AGN – IC 310, in favour of emission from the source's central SMBH [57].

The small-scale relativistic blobs in the "jet-in-jet" type models are moving with respect to the observer with the Lorentz factor $\Gamma_b^{tot} = \Gamma_b\Gamma_j$, where Γ_j and Γ_b are the Lorentz factors of the jet and the blob with respect to the jet correspondingly. The small size of the blobs ($\sim 10^{14}$ cm), compared to the size of the jet (~ 1 pc), requires them to be highly relativistic with $\Gamma_b^{tot} \sim 100$ in order to compete with the emission of the rest of the much larger jet through the Doppler booting of the flux. The relativistic movements of the blobs, as seen by the distant observer, result in the apparent superluminal motion with the speed β_{app}:

$$\beta_{app} = \beta \sin\theta / (1 - \beta \cos\theta) \tag{2}$$

where θ is the angle between the line of sight and direction of the blob movement and $\beta = \sqrt{1 - 1/\Gamma_b^{tot2}}$ is velocity of the blob. As the blazar jets are closely aligned with the line of sight, the typical value θ should be close to the opening angle of the jet $\sim 5°$. Assuming a typical value of $\Gamma_{tot} \sim 100$ we obtain $\beta_{app} \sim 10$. Such apparent superluminal motion of the source should lead to a very short caustics crossings time scale, which would be shorter than the minimal time scale present in the data: the duration of the sub-flares in different flaring episodes which is $\lesssim 1$ day. The increase of the magnification factor on the daily time scales would be possible only if the blob size is large enough, $R_b > \beta_{app}c \times (1)$ d $\sim 3 \times 10^{16}$ cm. However, this size is larger than the size of the Einstein rings of the stars in the lensing galaxy $R_E^* \simeq 4 \times 10^{16}\sqrt{M_*/M_\odot}$ so that no additional magnification due to microlensing would be possible at a all. Thus, the jet-in-jet models of the fast variability of gamma-ray emission from blazars are inconsistent with the detection of microlensing in PKS 1830-211.

Difficulties of the models in which the emission is produced at large distances from the SMBH implicitly favour the most "natural" possibility of emission coming from a stationary, compact source at the base of the AGN jet, in the direct vicinity of the central SMBH.

References

[31] Evans, P. A. *et al.* Methods and results of an automatic analysis of a complete sample of Swift-XRT observations of GRBs. *MNRAS* **397**, 1177-1201 (2009).

[32] Krimm, H. A. *et al.* The Swift/BAT Hard X-Ray Transient Monitor. *ApJS* **209**, id.14 (1-33) (2013).

[33] Courvoisier, T. J.-L. *et al.* The INTEGRAL Science Data Centre (ISDC). *A&A* **411**, L53-L57 (2003).

[34] Zhang, S. *et al.* High-Energy Properties of PKS 1830-211. *ApJ* **683**, 400-408 (2008).

[35] Mattox, J. R. *et al.* The Likelihood Analysis of EGRET Data. *ApJ* **461**, 396-407 (1996).

[36] Simonetti, J. H., Cordes, J. M. & Heeschen, D. S. Flicker of extragalactic radio sources at two frequencies. *ApJ* **296**, 46-59 (1985).

[37] Favre, P., Courvoisier, T. J.-L. & Paltani, S. AGN variability time scales and the discrete-event model. *A&A* **443**, 451-463 (2005).

[38] Savchenko, V., Neronov, A. & Courvoisier, T. J.-L. Timing properties of gamma-ray bursts detected by SPI-ACS detector onboard INTEGRAL. *A&A* **541**, A122 (1-8) (2012).

[39] Vovk, I. & Neronov, A. Variability of Gamma-Ray Emission from Blazars on Black Hole Timescales. *ApJ* **767**, id.103 (1-8) (2013).

[40] Emmanoulopoulos, D., McHardy, I. M. & Uttley, P. On the use of structure functions to study blazar variability: caveats and problems. *MNRAS* **404**, 931-946 (2010).

[41] Abdo, A. A. *et al.* Gamma-Ray Flaring Activity from the Gravitationally Lensed Blazar PKS 1830–211 Observed by Fermi LAT. *ApJ* **799**, id143 (2015).

[42] van Ommen, T. D., Jones, D. L., Preston, R. A. & Jauncey, D. L. Time delay in the Einstein ring PKS 1830-211. *ApJ* **444**, 561-566 (1995).

[43] Wiklind, T. & Combes, F. Time Delay of PKS 1830-211 Using Molecular Absorption Lines. In Brainerd, T. G. & Kochanek, C. S. (eds.) *Gravitational Lensing: Recent Progress and Future Go*, vol. 237 of *Astronomical Society of the Pacific Conference Series*, 155-156 (2001).

[44] Kayser, R., Refsdal, S. & Stabell, R. Astrophysical applications of gravitational micro-lensing. *A&A* **166**, 36-52 (1986).

[45] Schneider, P. & Weiss, A. The two-point-mass lens - Detailed investigation of a special asymmetric gravitational lens. *A&A* **164**, 237-259 (1986).

[46] Schneider, P. & Weiss, A. A gravitational lens origin for AGN-variability? Consequences of micro-lensing. *A&A* **171**, 49-65 (1987).

[47] Bate, N. F., Fluke, C. J., Barsdell, B. R., Garsden, H. & Lewis, G. F. Computational advances in gravitational microlensing: A comparison of CPU, GPU, and parallel, large data codes. *New Astronomy* **15**, 726-734 (2010).

[48] Chabrier, G. Galactic Stellar and Substellar Initial Mass Function. *Pub. Ast. Soc. of Pacific* **115**, 763-795 (2003).

[49] Bromberg, O. & Levinson, A. Recollimation and Radiative Focusing of Relativistic Jets: Applications to Blazars and M87. *ApJ* **699**, 1274-1280 (2009).

[50] Stawarz, L. *et al.* Dynamics and high-energy emission of the flaring HST-1 knot in the M 87 jet. *MNRAS* **370**, 981-992 (2006).

[51] Nakamura, M., Garofalo, D. & Meier, D. L. A Magnetohydrodynamic Model of the M87 Jet. I. Superluminal Knot Ejections from HST-1 as Trails of Quad Relativistic MHD Shocks. *ApJ* **721**, 1783-1789 (2010).

[52] Tavecchio, F. & Ghisellini, G. Spine-sheath layer radiative interplay in subparsec-scale jets and the TeV emission from M87. *MNRAS* **385**, L98-L102 (2008).

[53] Giannios, D., Uzdensky, D. A. & Begelman, M. C. Fast TeV variability in blazars: jets in a jet. *MNRAS* **395**, L29-L33 (2009).

[54] Ghisellini, G. & Tavecchio, F. Rapid variability in TeV blazars: the case of PKS2155-304. *MNRAS* **386**, L28-L32 (2008).

[55] Ghisellini, G., Tavecchio, F., Bodo, G. & Celotti, A. TeV variability in blazars: how fast can it be? *MNRAS* **393**, L16-L20 (2009).

[56] Narayan, R. & Piran, T. Variability in blazars: clues from PKS 2155-304. *MNRAS* **420**, 604-612 (2012).

[57] Aleksić, J. *et al.* Black hole lightning due to particle acceleration at subhorizon scales. *Science* **346**, 1080-1084 (2014).